Available online at www.sciencedirect.com
SCIENCE DIRECT®
International Journal of Engineering Science 42 (2004) 1439–1457
International Journal of Engineering Science
www.elsevier.com/locate/ijengsci

Enhancement of epitaxial lateral overgrowth by vapor-phase diffusion

M. Khenner

Department of Mathematics, State University of New York at Buffalo, 244 Mathematics Building, SUNY Buffalo, North Campus, Buffalo, NY 14260-2900, USA

Received 18 July 2003; received in revised form 12 December 2003; accepted 8 March 2004

(Communicated by G. LUKASZEWICZ)

Abstract

The mathematical model for vapor-phase diffusion-assisted epitaxial lateral overgrowth in homoepitaxy of a compound semiconductor (GaAs-type) thin film is presented. Besides diffusion in vapor phase, the physical mechanisms contributing to the crystal growth and accounted for in the model include surface diffusion and evaporation–recondensation. The evolution equations for the concentrations of bulk and surface species, and for the interface shape are solved by a combination of a finite difference and boundary element methods. Comparison of the results of the modeling to the models that ignore diffusion in vapor shows that the latter enhances the overgrowth on the mask; the degree of this enhancement increases with the widths of the stripe openings in the mask and of the masked regions.
© 2004 Elsevier Ltd. All rights reserved.

Keywords: CVD; Thin films; Compound semiconductors; Bulk and surface diffusion; Interface dynamics

1. Introduction

Epitaxial lateral overgrowth (ELO) and selective area epitaxy (SAG) are commonly used to grow micro-scale semiconductor crystals and thin films, which then find a broad range of applications in special device structures such as buried heterostructure lasers, electroadsorption modulators, light-emitting diodes, etc. [1,2]. Micrometer-scale selective growth is well achievable

E-mail address: mkhenner@nsm.buffalo.edu (M. Khenner).

0020-7225/$ - see front matter © 2004 Elsevier Ltd. All rights reserved.
doi:10.1016/j.ijengsci.2004.03.006

by MOCVD, MOVPE, or LPE [1–9]; moreover, recent reports demonstrate that ELO and SAG techniques can be used to grow nanostructures by MBE [10–12].

The advances in experimental field of SAG stimulate the interest in fundamental understanding of this specific crystal growth process. A number of models have been developed during the last decade which consider diffusion processes in vapor phase [1,13,14], in vapor phase and on a mask surface [15,16] or in vapor phase and on crystal surface [6]. While these models are quite successful in predicting the observed growth rates and usually contain only few parameters, they omit process(es) which are considered to be of secondary importance under specific realization of the crystal growth conditions. More striking is perhaps the fact that these models do not allow studies of evolutions of crystal shapes during the growth; these shapes are, generally, very anisotropic [1,8] and are of a primary interest for industrial applications.

Recently, mathematical models were introduced that allow to numerically study the ELO and SAG from vapor [17,18]. These models are formulated as free-boundary problems in two dimensions (that is, normal to the substrate/mask and normal to the axis of long stripe openings etched in the mask) and, therefore, they explicitly take into account the mask topography [17,18] and the crystal surface anisotropy [18]. The models take surface diffusion along the mask and on the crystal surface as dominant crystal growth mechanism and ignore diffusion in vapor phase; the effect of vapor phase is reduced to the *constant*, uniform supply of precursors to the mask and crystal surfaces. In the models, the normal velocity at any point on the crystal surface is a function of the curvature and its derivatives; marker points on the surface are advanced using parametric evolution equations for those points which use the normal velocity function. Every advancing step is followed by remeshing to have an even spacing between markers. The details of the numerical algorithm appear in [17]; the latter is similar to that of Wong et al. [19]. Models do not assume that there is or is not lateral overgrowth a priori; the overgrowth occurs naturally during the computation.

With both models, the qualitative agreement with experiment was observed. As the crystal grows onto the mask, a region of enhanced growth (''bump'') may form near the contact point; it is subsequently smoothed by diffusion on the crystal surface. The anisotropic properties (surface diffusion, energy and mobility) can greatly exaggerate the formation of distortions or bumps at the crystal edge, and the resulting shapes show striking resemblance to some grown crystals reported in the literature [1,8]. It was shown in [17] that the extent of the overgrowth onto the mask and the height of the crystal at the middle of the stripe depend on widths of the stripe and masked region. In particular, larger mask width results in larger crystal thickness [1,6,9], but larger stripe width results in smaller thickness. The height of the bump depends on the value of the contact angle between the crystal surface and the mask as well as on the widths of the stripe and masked regions. In [18], it was also demonstrated that some choices of parameters may lead to almost complete suppression of ELO or, on the contrary, to significant enhancement of ELO at the expense of vertical growth. Thus, this model offers a way to quantify the effect of orienting the growing crystal compared to the substrate, and to possibly understand how to control the shape of the growing crystal.

In this paper, the anisotropic model of [18] is extended to include diffusion in vapor phase. Influence of the diffusion in vapor on crystal shapes and growth rates is systematically studied over the wide range of mask and stripe widths and comparisons are made with the results of the ''constant-supply'' models of [17,18]. Note that the new model is still formulated as ''local'', or ''geometric'' model [20]; conditions that permit such formulation are discussed in the next section.

The paper proceeds as follows. The new model is formulated in Section 2. Numerical methods are briefly discussed in Section 3, and Section 4 gives numerical results. Section 5 contains the conclusions.

2. Model

Sketch of the mathematical situation is shown in Fig. 1. The length of the stripes is assumed much larger than their widths since large aspect ratios are common in the experiments; thus, 2D approximation can be used. Due to the periodic arrangement of the stripes, we examine the growth behavior on a partial cross-section which is a line segment extending from the center line of one mask surface at $x' = -\ell$ to the center of the adjacent stripe at $x' = L$. The mask is assumed to be of zero thickness since the objective of this paper is evaluation of the influence of vapor-phase diffusion on ELO in the long run. This approximation is made because usually the mask thickness ($\sim$0.1 μm) is much smaller than the mask width ($\sim$5 μm at least) and thus time needed to fill a stripe with crystal is much less than the total time for the overgrowth. Extension of the model to the case of nonzero mask thickness is straightforward.

2.1. Diffusion in vapor

Following the previous modeling efforts [1,6], [13–15], diffusion in boundary layer is considered steady state, since it was shown in the cited works with compelling evidence that such approximation leads to models which quite accurately match crystal growth rates and growth rate

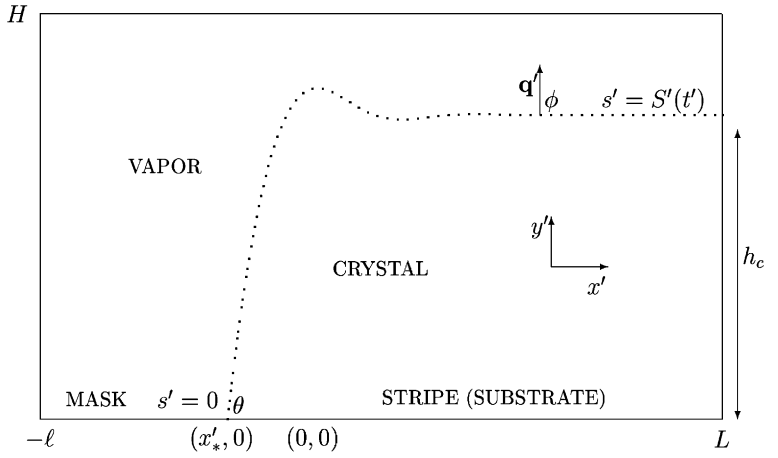

Fig. 1. A sketch of the mathematical situation. The free surface of the growing crystal (curve in two dimensions) is defined parametrically as $y' = y'(s', t')$, $x' = x'(s', t')$, $0 \leqslant s' \leqslant S'(t')$, where s' is the arc length along the curve and S' is the total arc length of the curve (primes denote dimensional variables). The surface is sketched such that a crystal overgrowth onto the mask is shown. ϕ is the angle that the unit normal, $\mathbf{q}'$, makes with the horizontal axis. Height of boundary diffusion layer above the substrate is H, and h_c denotes crystal height at the center of the stripe.

enhancement factors over wide range of experimental growth conditions and growth times. Therefore, the equation that describes diffusion in vapor is Laplace's equation

$$D_{\mathrm{v}}\left(\frac{\partial^2 n'_{\mathrm{v}}}{\partial (x')^2}+\frac{\partial^2 n'_{\mathrm{v}}}{\partial (y')^2}\right)=0, \tag{2.1}$$

where D_{v} is diffusion coefficient, and n'_{v} is concentration of metal-organic precursors. Boundary conditions are specified in Section 2.4.

2.2. Surface diffusion over the mask

The interval $-\ell \leqslant x' \leqslant 0$, $y'=0$ corresponds to the masked area of the substrate. Here we study the surface diffusion of the concentration $n'_{\mathrm{m}}=n'_{\mathrm{m}}(x',t')$ of adatoms on the horizontal part of the mask not yet covered by the growing crystal:

$$\frac{\partial n'_{\mathrm{m}}}{\partial t'}=D_{\mathrm{s}}^{(\mathrm{m})}\frac{\partial^2 n'_{\mathrm{m}}}{\partial (x')^2}+J'_i, \quad -\ell \leqslant x' \leqslant x'_*(t'). \tag{2.2}$$

In (2.2), J'_i is the net impinging flux of atoms from a vapor (explicit form for the flux is given in Section 2.4). $D_{\mathrm{s}}^{(\mathrm{m})}$ is the surface diffusivity of adatoms on the mask. Diffusion equation (2.2) is commonly used for modeling surface diffusion on crystal and mask surfaces in MBE and CVD (Ref. [15,21,22], for example).

Appended to (2.2) is a symmetry boundary condition,

$$\left.\frac{\partial n'_{\mathrm{m}}}{\partial x'}\right|_{(-\ell,t')}=0. \tag{2.3}$$

We assume that the adatoms close to the crystal will be absorbed quickly; thus we take the boundary condition at the contact point to be a perfect sink:

$$n'_{\mathrm{m}}(x'_*(t'),t')=0. \tag{2.4}$$

The initial condition is chosen $n'_{\mathrm{m}}(x',0)=0$, $-\ell \leqslant x \leqslant 0$.

2.3. Model for the crystal surface

In this section, an expression for the normal velocity $V'_{q'}$ of the interface between the crystal that builds-up from the substrate on the interval $0 \leqslant x' \leqslant L$, $y'=0$ and the vapor is provided, as well as boundary and initial conditions for the parametric evolution equations that use $V'_{q'}$ to evolve the interface (these equations are given in the nondimensional form in the Section 2.5). The interface is allowed to move above the mask on the interval $-\ell \leqslant x' < 0$, $y'=0$. The formulation presented here has its foundation in the classical work of Mullins [23] on grain boundary grooving by surface diffusion and evaporation–recondensation; it differs from one in [17,18] in that vapor-phase diffusion is now allowed to contribute to $V'_{q'}$.

It is important to mention that the influence of interface (crystal surface) motion on diffusion in vapor is almost completely ignored in our modeling; see note in the algorithm (Section 3). Thus "new" model still belongs to the class of *local* or *geometric* models of crystal growth [20]. Geometric models are defined in [20] as such in which the normal velocity of the surface depends only on the position of the surface, its local shape and on values that field variables (e.g., concentration n'_v) take on the surface if these values do not depend on concentration gradients created by surface motion and modified by diffusion in vapor. We believe that ELO of semiconductor crystals from vapor can be adequately described within the framework of a geometric model due to following reasons:

- As noted above, models of ELO developed in [1,6], [13–16] all assume steady-state diffusion field ahead of the interface. The predictions of the models (growth rates and growth enhancement factors) were matched to experimental results also reported in these works, with matching usually quite good over the wide range of growth times. Note that crystal growth conditions and experimental setups vary significantly in the mentioned experiments.
- Experimental crystal growth rates are small (<2 μm/h), which is characteristic for low-pressure ($\leqslant 1$ atm) MOCVD/MOVPE reactors [1,6], [13–16]. On the other hand, the height of a convection-free, diffusion boundary layer is several hundred microns [15]. It is therefore unlikely that such a slow surface motion produces large concentration gradients in the vapor.
- Complex crystal structures, such as those observed in dendritic solidification (for some examples of theoretical and computational approaches, see [24–31]) and that are known to be a result of morphological instability induced by nonstationary gradients of temperature and concentration at the interface were never reported for ELO.

Interface motion in new model is driven by a net normal flux of precursors at the interface from/to the vapor and by surface diffusion of adatoms along the interface. The contribution of first driving force to normal velocity is proportional to the jump in the chemical potential across the interface, viz.

$$M\frac{n'_s}{k_B T}(\mu_v - \mu_c), \tag{2.5}$$

where M is interface mobility, n'_s is surface concentration (the number of adatoms per unit area of the interface), k_B is Boltzman's constant, T is temperature, μ_v is chemical potential of the interfacial layer on vapor side and $\mu_c = \Omega\gamma K'$ is chemical potential of the interfacial layer on crystal side (where Ω is atomic volume, γ is crystal-vapor surface energy and K' is curvature). Note that given form of μ_c assumes isotropic surface energy, e.g. γ does not depend on crystal surface orientation ϕ. Here and below the isotropic γ is chosen to reduce the number of parameters to the model; influence of mildly anisotropic γ was studied in [18].

To determine μ_v, we make use of the definition of the diffusivity in vapor [32]:

$$D_v = \chi\left(\frac{\partial\mu_v}{\partial n'_v}\right)_{T,P}, \tag{2.6}$$

where χ is a positive proportionality constant. From (2.6), requiring that at $y' = H : \mu = \mu_\infty = \text{const.} \neq \mu_\text{v}$ and choosing χ that corresponds to zero equilibrium (reference) value of the chemical potential, it follows that

$$\mu_\text{v} = \frac{n'_\text{v}}{n_\infty}\mu_\infty. \tag{2.7}$$

The second contribution is from the surface diffusion of atoms along the interface; the current of atoms J_s is proportional to the surface gradient of μ_c. For the curve in the plane, the surface gradient is the derivative with respect to arc length, hence

$$J_\text{s} = -\frac{n'_\text{s}}{k_\text{B}T}D_\text{s}^{(\text{c})}\frac{\partial\mu_\text{c}}{\partial s'}, \tag{2.8}$$

where $D_\text{s}^{(\text{c})}$ is coefficient of diffusion on crystal surface. The contribution to the rate of increase in the atoms per unit length (proportional to the normal velocity) is proportional to $(-\partial J_\text{s}/\partial s')$. Combining the vapor and surface diffusion contributions results in

$$V'_{q'} = \frac{\Omega}{k_\text{B}T}\left\{\Omega\gamma\frac{\partial}{\partial s'}\left[D_\text{s}^{(\text{c})}n'_\text{s}\frac{\partial K'}{\partial s'}\right] + Mn'_\text{s}\left(\frac{n'_\text{v}|_\text{interface}}{n_\infty}\mu_\infty - \Omega\gamma K'\right)\right\}. \tag{2.9}$$

The first term in (2.9) is due to surface diffusion, and the third term is due to evaporation–recondensation. Second term is due to the impinging flux from vapor on the interface. Surface concentration is taken as

$$n'_\text{s} = \eta_\text{s}^{-1}n'_\text{v}|_\text{interface}, \tag{2.10}$$

where η_s is the parameter with units length^{-1}. n'_s is thus a function of the position on the interface and of the time, since the solution n'_v of the diffusion problem in vapor phase at any point in vapor domain (including the interface) is time dependent due to interface motion and deformation, as well as due to dynamic boundary conditions (2.18) and (2.19) (Section 2.4). (2.9) is more general than the expressions for the normal velocity used in [17,18]; there, *mean* surface concentration $n'_\text{s} \equiv v = \text{const.}$ (or constant effective thickness of the interfacial layer $\delta = \Omega n'_\text{s}$ [23]) was assumed.

Anisotropic evolution of the crystal surface is accounted for by postulating the dependence of M and $D_\text{s}^{(\text{c})}$ on crystal surface orientation given by the angle of the unit normal, ϕ, to the surface:

$$M = M_0\hat{M}(\phi), \quad D_\text{s}^{(\text{c})} = D_0\hat{D}(\phi), \tag{2.11}$$

where M_0, D_0 are mean values. $\hat{M}(\phi), \hat{D}(\phi)$ are given by

$$\begin{aligned}\hat{M}(\phi) &= 1 + \epsilon_\text{m}\cos[4(\phi + \beta_\text{m})],\\ \hat{D}(\phi) &= 1 + \epsilon_\text{d}\cos[4(\phi + \beta_\text{d})],\end{aligned} \tag{2.12}$$

where (i) constants $\epsilon_\text{m}, \epsilon_\text{d}$ $(0 \leqslant \epsilon_\text{m},\ \epsilon_\text{d} \leqslant 1)$ determine the degree of the anisotropy of M and $D_\text{s}^{(\text{c})}$, respectively, (ii) β_m and β_d are phase angles. In (2.12), four-fold anisotropy is assumed; formulas of this type are often used to model anisotropic crystal growth.

Next, physical boundary and initial conditions that augment the evolution problem for the interface are described. These conditions are same as in [17,18].

First, the contact angle $\theta(\gamma, \gamma_{\rm cm}, \gamma_{\rm mv})$ which the crystal surface forms with the mask at the contact point is constant as a result of the thermodynamic equilibrium at the junction [33]. Here $\gamma_{\rm cm}$ and $\gamma_{\rm mv}$ are respectively the crystal-mask and mask-vapor surface energies, and θ is thus a material parameter. The condition reads

$$\theta = \text{const.} \quad \text{at } x' = x'_*(t'). \tag{2.13}$$

Symmetry conditions on the shape of the crystal are prescribed at $x' = L$,

$$\left.\frac{\partial y'}{\partial x'}\right|_{(L,t')} = 0 \quad \text{and} \quad \left.\frac{\partial^3 y'}{\partial (x')^3}\right|_{(L,t')} = 0; \tag{2.14}$$

these conditions prevent any flux of atoms across $x' = L$.

Initially, the crystal surface is assumed to be a hyperbolic tangent curve that has the contact angle $\theta_0 < 90^\circ$ with the mask at the contact point:

$$y'(s',0) = y'_0\left[1 - \tanh\left(s'\frac{\tan\theta_0}{y'_0}\right)\right], \qquad x'(s',0) = s', \quad 0 \leqslant s' \leqslant L. \tag{2.15}$$

In (2.15), y'_0 is a small constant which gives the initial thickness of the crystal at $x' = L$.

The slope of the interface at the contact point for $t' > 0$ is given by

$$\left.\frac{\partial y'}{\partial x'}\right|_{(x'_*(t'),t')} = \tan\theta. \tag{2.16}$$

The surface diffusion flux on the mask is matched with the flux onto the growing crystal by requiring, at $x' = x'_*$ and t', that

$$D_{\rm s}^{(\rm m)}\frac{\partial n'_{\rm m}}{\partial x'} = \frac{n'_{\rm s}}{k_{\rm B}T}D_{\rm s}^{(\rm c)}\Omega\gamma\frac{\partial K'}{\partial s'}. \tag{2.17}$$

2.4. Boundary conditions for the Laplace's Eq. (2.1)

Concentration at the top of the diffusion layer (at $-\ell \leqslant x' \leqslant L$, $y' = H$) is prescribed, $n'_{\rm v} = n_\infty$. $\partial n'_{\rm v}/\partial x' = 0$ at left and right boundaries of vapor phase (at $x' = -\ell$, $0 < y' < H$ and at $x' = L$, $h_{\rm c} < y' < H$) due to symmetry of the problem.

The difference of impinging and evaporation–recondensation fluxes at the mask and at the crystal–vapor interface provides the last two boundary conditions for (2.1):

$$-\ell \leqslant x' \leqslant x'_*(t'),\ y' = 0: \qquad D_{\rm v}\frac{\partial n'_{\rm v}}{\partial y'} = \sigma_{\rm m}J_{\rm g} - \frac{n'_{\rm m}}{\tau_{\rm m}} \equiv J'_i; \tag{2.18}$$

Table 1
Physical parameters

Constant	Description	Value/units
J_g	Atomic flux from vapor	10^{15} atoms/(cm^2 s)
τ_m	Mean residence time of atoms on mask	0.1 s
σ_m	Sticking coefficient on mask	1.0
D_v	Diffusivity in vapor	3×10^{-6} cm^2/s
$D_s^{(m)}$	Diffusivity on mask	5×10^{-8} cm^2/s
D_0	Mean diffusivity on crystal surface	2×10^{-8} cm^2/s
Ω	Atomic volume	2×10^{-23} cm^3/atom
γ	Surface energy	10^3 ergs/cm^2
μ_∞	Chem. pot. in the far field (at $y' = H$)	3×10^{-13} erg/atom
M_0	Mean mobility	10 s^{-1}
L	Width of substrate region	5×10^{-4}–3×10^{-3} cm (5–300 μm)
ℓ	Width of mask region	5×10^{-4}–3×10^{-3} cm (5–300 μm)
H	Thickness of diffusion boundary layer	10^{-2} cm (100 μm)
n_∞	Vapor concentration at $y' = H$	8×10^{18} atoms/cm^3
θ	Equilibrium contact angle	120°
θ_0	Initial contact angle	60°

$$0 \leqslant s' \leqslant S'(t') : \qquad D_v \frac{\partial n'_v}{\partial q'} = J_g\left(1 - \frac{\gamma\Omega K'}{k_B T}\right). \tag{2.19}$$

In (2.18), $0 < \sigma_m \leqslant 1$ is sticking coefficient on the mask; this is new parameter absent from previous models [17,18] (sticking coefficient on the interface is assumed unity [15]). The term n'_m/τ_m accounts for the loss of adatoms due to desorption. The constant τ_m is the mean adatom residence time on the mask. The form of J_g is usually given by the kinetic theory of gases, as follows:

$$J_g = \frac{P_0}{(2\pi m k_B T)^{1/2}}. \tag{2.20}$$

In (2.20), P_0 is vapor pressure, m is molecular weight and k_B is Boltzman's constant. (2.18), (2.19) are equivalent to the assumption of the first order reaction rate [15,23,32]. For the purpose of direct comparison with the model without the diffusion in the vapor, we take here value for J_g as in [18] (Ref. Table 1).

2.5. Nondimensional problem

The physical constants listed in Table 1 are representative for ELO of GaAs-like material at temperatures near 650 °C.

Next, the model equations are nondimensionalised using same scales as in [17]; two additional scales which arise due to diffusion in vapor are

$$n'_v = n_\infty n_v, \qquad n'_s = \frac{L^2}{D_s^{(m)}} J_g n_s. \tag{2.21}$$

Table 2
Nondimensional parameters

Constant	Expression	Value ($L = 5$, $\ell = 20$ μm)	Value ($L = 30$, $\ell = 120$ μm)
Z	$(\Omega^2 J_g \gamma D_0)/(D_s^{(m)^2} k_B T)$	2.5×10^{-8}	2.5×10^{-8}
Y	$(\Omega \mu_\infty J_g M L^3)/(D_s^{(m)^2} k_B T)$	2.35×10^{-2}	5.08
X	$(\Omega^2 J_g \gamma M L^2)/(D_s^{(m)^2} k_B T)$	3×10^{-6}	1.1×10^{-4}
W	$(\Omega L \gamma D_0)/(D_s^{(m)^2} \tau_m k_B T)$	6.3×10^{-3}	3.8×10^{-2}
Λ	$(J_g L)/(D_v n_\infty)$	2×10^{-2}	1.2×10^{-1}
U	$(\Omega J_g \gamma)/(D_v n_\infty k_B T)$	6×10^{-6}	6×10^{-3}
ω	$(D_v n_\infty L)/(\tau_m J_g D_s^{(m)})$	2.4×10^{3}	1.44×10^{4}
Γ_s	$(\eta_s L^2 J_g)/(n_\infty D_s^{(m)})$	1	1
$\bar{H}$	H/L	20	3.3
d	ℓ/L	4	4
y_0	y_0'/L	5×10^{-3}	5×10^{-3}

Table 2 contains estimates of the nondimensional parameters for two sets of the mask and stripe widths. These sets will be referred to as "narrow geometries" and "wide geometries", respectively. Notice that the nondimensional width of the mask, d, is same for both sets.

The nondimensional Laplace's Eq. (2.1) reads

$$\frac{\partial^2 n_v}{\partial x^2} + \frac{\partial^2 n_v}{\partial y^2} = 0, \tag{2.22}$$

with boundary conditions

$$\text{at} \quad -d \leqslant x \leqslant 1, \ y = \overline{H}: \quad n_v = 1; \tag{2.23}$$

$$\text{on the mask} \quad -d \leqslant x \leqslant x_*(t), \ y = 0: \quad \frac{\partial n_v}{\partial y} = \Lambda(\sigma_m - n_m) \equiv J_i; \tag{2.24}$$

$$\text{on the crystal surface } (0 \leqslant s \leqslant S(t)): \quad \frac{\partial n_v}{\partial q} = \Lambda - UK; \tag{2.25}$$

$$\text{at } x = -d, \ 0 < y < \overline{H} \quad \text{and at} \quad x = 1, \ h_c < y < \overline{H}: \quad \frac{\partial n_v}{\partial x} = 0, \tag{2.26}$$

where h_c now denotes the nondimensional thickness of the crystal in the center of the stripe.

The nondimensional diffusion problem on the mask is

$$\frac{\partial n_m}{\partial t} = \frac{\partial^2 n_m}{\partial x^2} + \omega J_i, \qquad \left.\frac{\partial n_m}{\partial x}\right|_{(-d,t)} = 0, \quad n_m(x_*(t), t) = 0, \ \ n_m(x, 0) = 0. \tag{2.27}$$

The nondimensional parametric evolution equations for the crystal surface are

$$\begin{aligned}\frac{\partial x}{\partial t} &= V_q \frac{\partial y}{\partial s},\\ \frac{\partial y}{\partial t} &= -V_q \frac{\partial x}{\partial s}.\end{aligned} \tag{2.28}$$

In (2.28), the nondimensional normal velocity is given by

$$V_q = Z\frac{\partial}{\partial s}\left[\hat{D}(\phi)\frac{\partial K}{\partial s}n_{\mathrm{s}}\right] + Y\hat{M}(\phi)n_{\mathrm{s}}n_{\mathrm{v}}|_{\mathrm{interface}} - X\hat{M}(\phi)Kn_{\mathrm{s}}, \tag{2.29}$$

where

$$n_{\mathrm{s}} = \Gamma_{\mathrm{s}}^{-1}n_{\mathrm{v}}|_{\mathrm{interface}}. \tag{2.30}$$

Natural value $\Gamma_{\mathrm{s}} = 1$ is taken for the computation. In (2.29), $\hat{M}(\phi)$, $\hat{D}(\phi)$ are given by (2.12) and

$$K = \frac{\partial^2 y}{\partial s^2}\frac{\partial x}{\partial s} - \frac{\partial^2 x}{\partial s^2}\frac{\partial y}{\partial s} \tag{2.31}$$

is the nondimensional curvature.

The nondimensional boundary conditions for Eq. (2.28) are (see Fig. 1; note that $x_*(t)$ corresponds to $s = 0$ at all times):

$$\left.\frac{\partial y}{\partial s}\right|_{(s=S(t),t)} = 0, \quad \left.\frac{\partial^3 y}{\partial s^3}\right|_{(s=S(t),t)} = 0, \tag{2.32}$$

$$\left.\frac{\partial y/\partial s}{\partial x/\partial s}\right|_{(s=0,t)} = \tan\theta, \quad \theta = \mathrm{const}. \tag{2.33}$$

and

$$\left.\frac{\partial K}{\partial s}\right|_{(s=0,t)} = \frac{f_{\mathrm{m}}}{W\hat{D}(\phi_0)}. \tag{2.34}$$

In (2.34), ϕ_0 is the angle of the normal at $s = 0$; f_{m} is a surface diffusion flux from mask, which emerges from the numerical solution to initial-boundary value problem (2.27) with moving contact point $x_*(t)$. The solution procedure to obtain f_{m} is described in the appendix of [18]; it is also summarized in the next section. (2.34) is used to find the interface curvature at the contact point.

The nondimensional initial condition for Eq. (2.28) is

$$y(s,0) = y_0\left(1 - \tanh\left(s\frac{\tan\theta_0}{y_0}\right)\right), \qquad x(s,0) = s, \quad 0 \leqslant s \leqslant 1. \tag{2.35}$$

Here y_0 is a constant specifying the initial crystal thickness.

3. Numerical methods

Diffusion problem in vapor phase (2.22)–(2.26) is solved by a standard boundary element method [34], which allows to avoid discretization and solution in the bulk vapor. Linear elements were employed in this study.

Diffusion problem on the mask (2.27) is first mapped using transformation of variables $(x(t) \to \xi,\ n_{\mathrm{m}} \to N_{\mathrm{m}}(\xi, t))$ onto fixed interval $-d \leqslant \xi \leqslant 0$ [18] and discretized in ξ using finite differences. The resulting set of coupled ordinary differential equations in time is integrated by the standard ODE solver RADAU [35]. The solution yields the flux

$$f_{\mathrm{m}} = \left(\frac{-d}{d_1}\right) \left.\frac{\partial N_{\mathrm{m}}}{\partial \xi}\right|_{(\xi=0,t)} \tag{3.1}$$

of adatoms from the mask onto the crystal at the contact point. In (3.1), $d_1(t)$ is distance from the contact point to the center of the mask at $x = -d$:

$$d_1(t) = d - |x_*(t)|. \tag{3.2}$$

This flux is then used in the boundary condition (2.34). Also, the obtained concentration n_{m} is used in the boundary condition (2.24) on the next time level.

Evolution problem (2.28)–(2.35) is solved by a finite-difference method (namely, the marker particles method) described in [17]. The solution yields the surface profile (in the xy-plane), dynamically evolving in time.

Overall, the computational algorithm is as follows.

1. At $t = 0$, set $n_{\mathrm{m}} = 0$ along the mask. The RHS of (2.24) (J_i) is now known. Notice that the initial curvature at the RHS of (2.25) is also known, since the initial curve is given.
2. Solve problem (2.22)–(2.26) using BEM.
3. On the curve, set $n_{\mathrm{s}} = n_{\mathrm{v}}/\Gamma_{\mathrm{s}}$, where n_{v} is the solution of (2.22)–(2.26) on the crystal surface.
4. Update n_{m} on the mask from the diffusion problem on the mask, (2.27). Use this updated n_{m} to compute the RHS of (2.34), and then compute the curvature of the curve at the contact point using the one-sided finite-difference approximation.
5. On the curve, advance all marker particles except the one that coincides with the contact point, one time step forward. Update the position of the contact point using the contact angle condition (2.33). Now the curvature of this updated curve is different from the one at the previous time level. Use it to recompute the RHS of (2.25) (this is the only influence of the crystal–vapor interface on the diffusion in vapor). Also, use the updated concentration on the mask to recompute the RHS of (2.24). Then go to step 2.

Grids of two types used for discretizations along the boundaries are independent, thus allowing flexibility in choosing the number of grid nodes for possibly the most accurate solution of each subproblem. 200 boundary elements are employed on the interface, 100 on the mask and 50 on vertical and side boundaries of the computational box. The finite difference mesh on the mask contains 200 nodes, and the marker particles mesh on the interface has 500 nodes.

Communications between grids are performed using the parametric cubic spline interpolation. All computations were done on a single, 2.2 MHz Intel Xeon processor; typical run time to evolve the interface to 'final' nondimensional time $t_f = 3$ is 5 h. The code was compiled with Intel Fortran Compiler 7.0 for Linux.

4. Numerical results

In this section, the numerical results (obtained with the use of the "old" model of [18] and of the "new" model) are presented and compared. Since the parameter space is very large, only two distinct cases of the anisotropic growth were selected for a study. These are the cases of nonzero anisotropies of interface mobility and surface diffusion, as follows (Eq. (2.12)):

- Case 1:

$$\epsilon_m = \epsilon_d = 0.75, \qquad \beta_m = \beta_d = 0^\circ.$$

- Case 2:

$$\epsilon_m = \epsilon_d = 0.75, \qquad \beta_m = \beta_d = 45^\circ.$$

It was demonstrated in [18] that cases 1 and 2 with $\epsilon_m = \epsilon_d = 0.95$ provide two extreme regimes of ELO. In the first case, the overgrowth onto the mask is insignificant; however, a crystal with a close-to-pyramidal shape grows fast in the stripe. In the second case, growth in the stripe is slow; however, a thin crystal overgrows fast onto the mask. In this study, a moderate value of 0.75 was chosen for ϵ_m and ϵ_d for the reason of a reduced numerical stability of the algorithm with incorporated vapor-phase diffusion.

Results are presented for two sets of widths L and ℓ (Ref. Table 2). Intermediate widths between these two extremes were also employed in the course of study to ensure that transition in ELO properties occurs smoothly as widths increase from the lower to the upper bound. The nondimensional parameters of Table 2 were fixed at their cited values for the two sets of widths. In the end of this section we discuss the results obtained with $\sigma_m = 0.01$.

4.1. Crystal shapes

Fig. 2 shows the crystal shapes for growth in narrow geometries and for both models. Fig. 2(a) shows Case 1 growth with the crystal shapes at $t = 8i$, $i = 0, .., 4$; Fig. 2(b) shows Case 2 growth with the crystal shapes at the same times as Fig. 2(a).

In the Case 1, growth in narrow geometries (Fig. 2(a)), the crystals are imperfect pyramids with the curved sidewalls and shrinking top surfaces; by the final time $t_f = 32$ (when runs were terminated), this surface disappeared. Each model results in the approximately equal growth rates in lateral and vertical directions. [1]

[1] Note that scales along x, y coordinate axis at all figures in this paper are not equal.

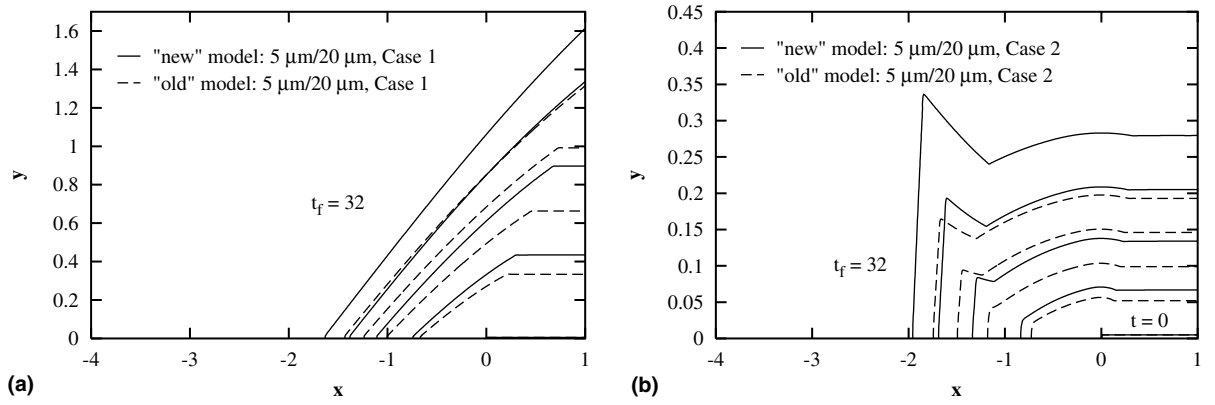

Fig. 2. Crystal shapes. (a) Case 1 growth in narrow geometries, both models. (b) Case 2 growth in narrow geometries, both models.

In the Case 2, growth in narrow geometries (Fig. 2(b)), the crystal shapes are macroscopically rough. The spike at the left end of the crystal is caused by the maximal mobility M in the direction 135° to the x-axis. The curved region between the spike and the flat right end of the curve is the successor of the bump which formed near the contact line at the initial stage of the growth [18]. Note that growth in the vertical direction is about 10 times slower than in the lateral one. The increase in the number of marker particles on the interface results in the smoother shapes, but also requires denser BEM grid in order to preserve the accuracy of the interpolation. Thus due to the computational time constraint the number of marker particles was fixed at 500.

Fig. 3 shows the crystal shapes for growth in wide geometries and for both models. Fig. 3(a) shows Case 1 growth with the crystal shapes at $t = 0, 1, 2$; Fig. 3(b) shows Case 2 growth with the crystal shapes at $t = 0, 1, 2, 3$.

In the Case 1, growth in wide geometries (Fig. 3(a)), the crystals are almost perfect pyramids; for each model, lateral and vertical growth rates do not differ much.

In the Case 2, growth in wide geometries (Fig. 3(b)), the crystal grows fast in the direction 135° to the x-axis as in the case of Fig. 2(b). Note, however, that the important property of the Case 2 growth in narrow geometries (that is, fast lateral overgrowth) is lost: the overgrowth distance by the final time is only approximately two times larger than the crystal height in the center of the stripe (at $x = 1$).

The rough comparison of Fig. 3 to Fig. 2 shows that the crystal growth in wide geometries is significantly faster than in narrow geometries. Also, growth governed by the new model with vapor phase diffusion is significantly faster than growth governed by the old model without this diffusion. The difference in growth rates between the new and the old model increases noticeably with time for growth in wide geometries. These effects are quantified in the next section.

4.2. Growth rates

Fig. 4 shows (for the crystal growth computed in Figs. 2, 3) the overgrowth distances on the mask vs. time, while the crystal heights in the center of the stripe are shown in Fig. 5.

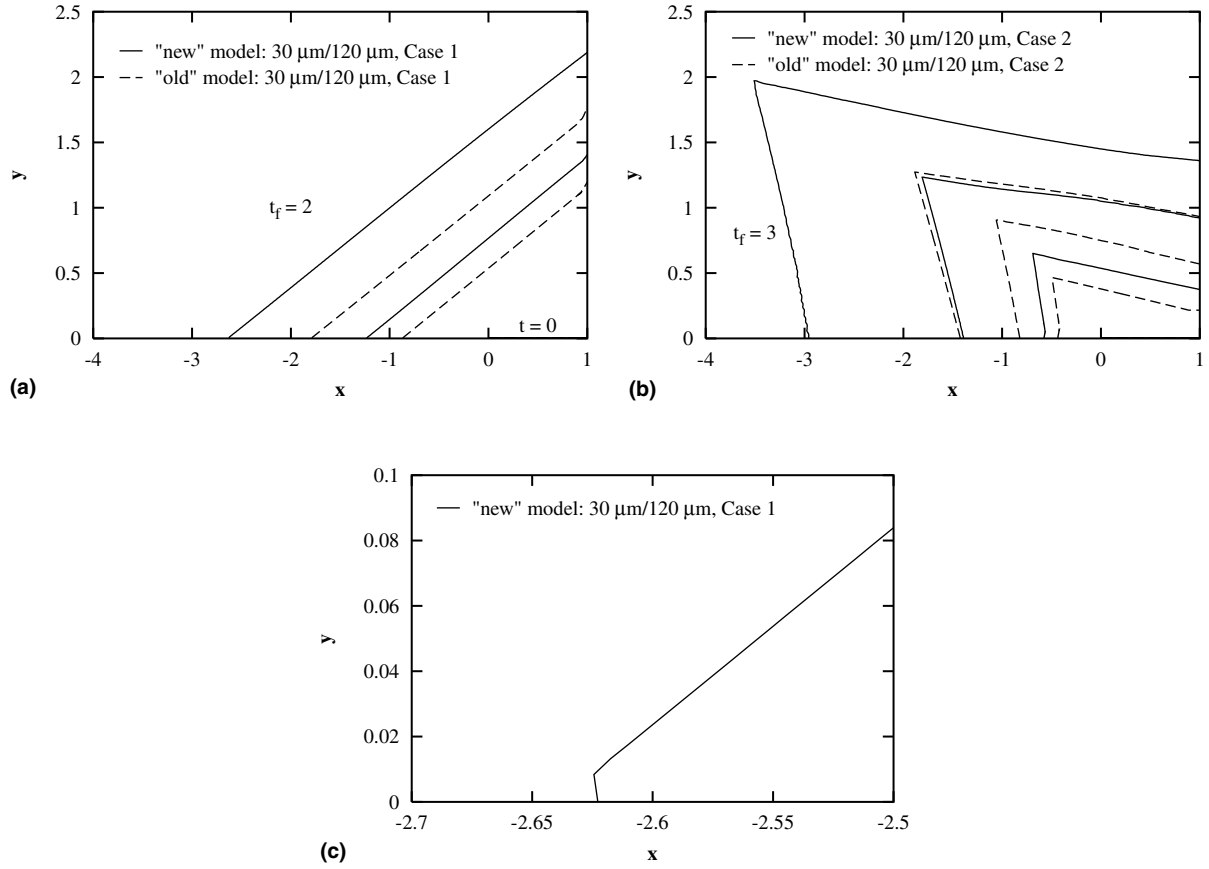

Fig. 3. Crystal shapes. (a) Case 1 growth in wide geometries, both models. (b) Case 2 growth in wide geometries, both models. (c) Zoom near the contact point of the last crystal shape in (a).

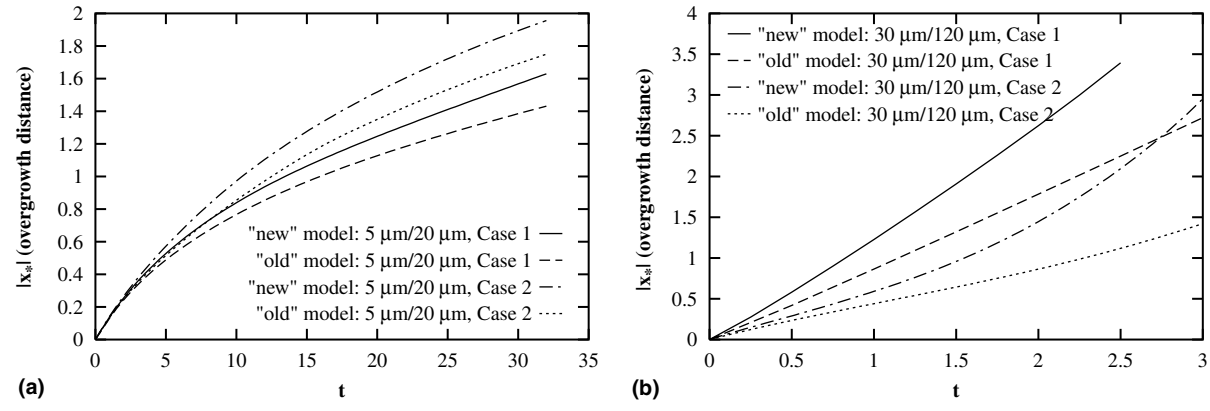

Fig. 4. (a) Overgrowth distance on the mask vs. time for the Case 1 and Case 2 growth in narrow geometries, both models. (b) Same as (a), but for wide geometries.

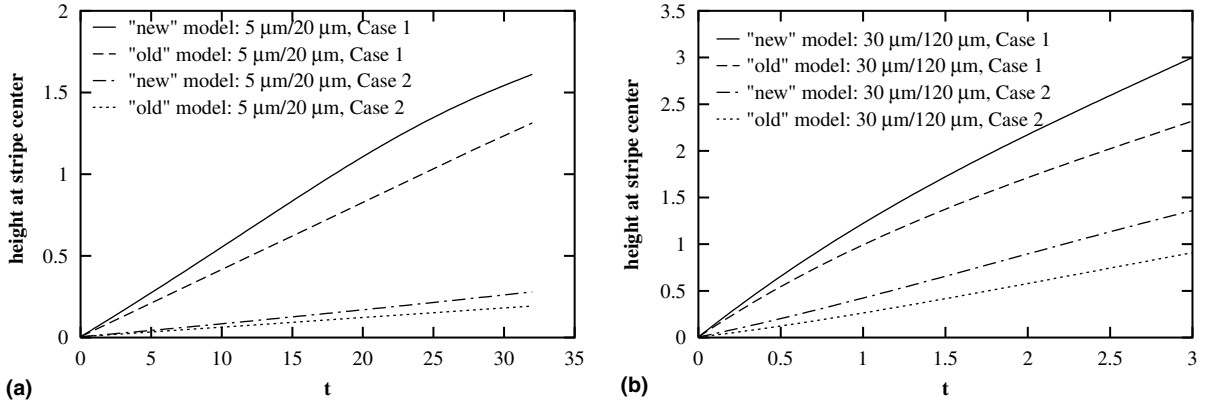

Fig. 5. (a) Crystal height at the center of the stripe for the Case 1 and Case 2 growth in narrow geometries, both models. (b) Same as (a), but for wide geometries. Solid line is extrapolated to $t = 3$ for visibility.

The vapor-phase diffusion model predicts (at any given time) the largest crystal height for the Case 1 and Case 2 growth in both narrow (Fig. 5(a)) and wide geometries (Fig. 5(b)). It also gives the largest overgrowth distance.

Also, the ratio of the "new" *vertical* growth rate to the "old" one increases with time faster for wide geometries (Fig. 5(b)) than for narrow geometries (Fig. 5(a)); same is true for the *overgrowth* rate.

Let $R_{\mathrm{l}}^{(\mathrm{w})}$ and $R_{\mathrm{l}}^{(\mathrm{n})}$ denote *average* (over the full time of each modeled crystal growth event) lateral growth rates predicted by the new model in wide and narrow geometries, respectively. Also, let $R_{\mathrm{v}}^{(\mathrm{w})}$ and $R_{\mathrm{v}}^{(\mathrm{n})}$ denote average vertical growth rates predicted by the new model in wide and narrow geometries, respectively. Then,

$$\frac{R_{\mathrm{l}}^{(\mathrm{w})}}{R_{\mathrm{l}}^{(\mathrm{n})}} \approx 26, \qquad \frac{R_{\mathrm{v}}^{(\mathrm{w})}}{R_{\mathrm{v}}^{(\mathrm{n})}} \approx 22 \tag{4.1}$$

for Case 1 growth, and

$$\frac{R_{\mathrm{l}}^{(\mathrm{w})}}{R_{\mathrm{l}}^{(\mathrm{n})}} \approx 16, \qquad \frac{R_{\mathrm{v}}^{(\mathrm{w})}}{R_{\mathrm{v}}^{(\mathrm{n})}} \approx 52 \tag{4.2}$$

for Case 2 growth. Thus, for Case 1 growth, the uniform increase of the widths L and ℓ results in almost uniform increase of the growth rates, while for Case 2 growth, the uniform increase of the widths results in much larger increase of the vertical growth rate than of the lateral growth rate. To quantify relative contribution of the width ℓ to the growth rates, the runs were performed with $L = 30$ and $\ell = 20$ (that is, keeping stripe width fixed but decreasing the mask width by a factor of six (in "wide geometries" case)). Denote the resulting average growth rates $R_{l}^{(\mathrm{w}/6)}$ and $R_{\mathrm{v}}^{(\mathrm{w}/6)}$. Then,

$$\frac{R_{l}^{(\mathrm{w}/6)}}{R_{\mathrm{l}}^{(\mathrm{w})}} \approx 1.1, \qquad \frac{R_{\mathrm{v}}^{(\mathrm{w}/6)}}{R_{\mathrm{v}}^{(\mathrm{w})}} \approx 2.26 \tag{4.3}$$

for Case 1 growth, and

$$\frac{R_l^{(w/6)}}{R_l^{(w)}} \approx 0.8, \qquad \frac{R_v^{(w/6)}}{R_v^{(w)}} \approx 0.92 \tag{4.4}$$

for Case 2 growth. Thus, decreasing mask width alone (or, in other words, increasing three-fold the ratio of the unmasked substrate area to the total substrate area) does not result in the pronounced effect on growth rates. Data suggests, however, that growth rates can be either slightly enhanced or reduced depending on the particular shape of the crystal grown.

Fig. 6 shows the surface diffusion flux f_m from the mask at the contact point vs. the length d_1 of the free portion of the mask. For growth in narrow geometries, the flux is practically constant; for growth in wide geometries, flux is larger and increases with overgrowth. It must be noted here that f_m contributes to the lateral growth rate only indirectly, and that influence is quite weak [18].

(See also next section. Same conclusion has been reached in [15]. In that work, the description of the diffusion on the mask lacks boundary condition at the mask center for the steady-state diffusion equation there. However, the incorporation of adatoms from the mask into the crystal growing in the window is given by the flux balance equation (6), that in our notation reads:

$$D_s^{(m)} \frac{dn'_m}{dx'}\bigg|_{\text{mask edge}} = k_s^{(m)} n'_m|_{\text{mask edge}},$$

where $k_s^{(m)}$ is the first order reaction rate constant. The latter equation also serves as boundary condition at the mask edge. The following is stated in [15] (p. 588): "The rate constant, being largely unknown, was varied over several orders of magnitude and found to have a negligible influence on the net flux to the window. ... These results suggest that direct diffusion from the gas phase accounts for nearly all of the excess reactant supply to the exposed window area in selective epitaxy". Note that in [15] ELO was not considered and the solution of the free boundary problem for the crystal was not attempted.)

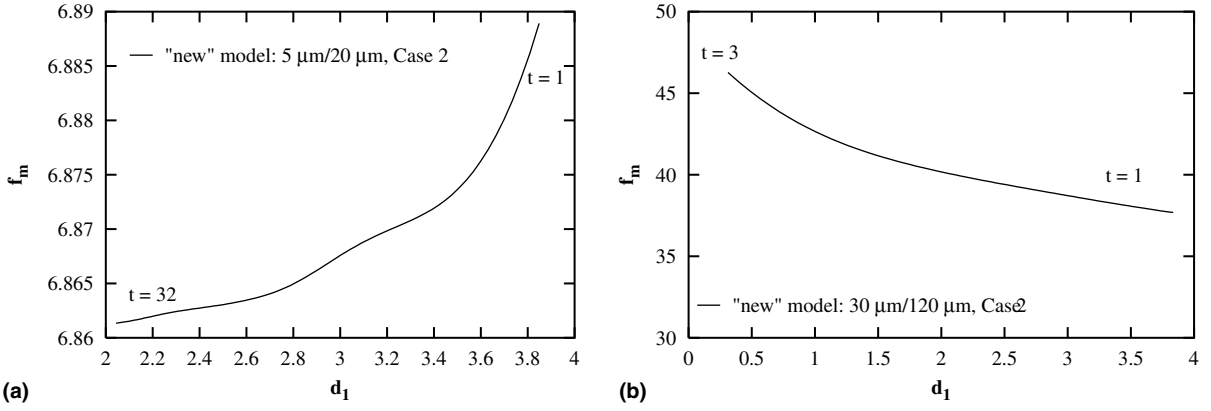

Fig. 6. (a) Flux of adatoms from the mask onto the overgrowing crystal vs. distance from the contact point to the mask center for the Case 2 growth in narrow geometries (new model). (b) Same as (a), but for wide geometries.

Indeed, in our model f_{m} is used only to evaluate the curvature of the interface at the contact point; this value is needed for the computation of the normal velocity at adjacent marker points on the interface, but the contact point. The location of the contact point is determined by coordinate's extrapolation using the contact angle condition.

4.3. Case of sticking coefficient $\sigma_{\mathrm{m}} = 0.01$

The steady-state diffusion problem on the mask (Eq. (2.27))

$$\frac{\mathrm{d}^2 n_{\mathrm{m}}}{\mathrm{d}x^2} - \alpha n_{\mathrm{m}} = -\alpha\sigma_{\mathrm{m}}, \qquad \left.\frac{\mathrm{d}n_{\mathrm{m}}}{\mathrm{d}x}\right|_{(-d,t)} = 0, \quad n_{\mathrm{m}}(x_*(t)) = 0, \quad \alpha \equiv \omega\Lambda$$
$$= \text{const.}, \quad -d \leqslant x \leqslant x_*(t) \tag{4.5}$$

has solution

$$n_{\mathrm{m}} = \sigma_{\mathrm{m}}\left[1 - \frac{\mathrm{e}^{2d\sqrt{\alpha}}\mathrm{e}^{x\sqrt{\alpha}} + \mathrm{e}^{-x\sqrt{\alpha}}}{\mathrm{e}^{(d+d_1)\sqrt{\alpha}} + \mathrm{e}^{(d-d_1)\sqrt{\alpha}}}\right], \tag{4.6}$$

where d_1 is given by (3.2). Thus surface concentration is naturally uniformly proportional to sticking coefficient. Fig. 7 shows the exemplary concentration profiles that result from the solution of the full time-dependent problem (2.27) with $\sigma = 0.01$.

From (4.6), the flux at the contact point,

$$f_{\mathrm{m}} = \sigma_{\mathrm{m}}\sqrt{\alpha}\tanh(d_1\sqrt{\alpha}), \tag{4.7}$$

is also proportional to σ_{m}. In [18] it was shown (for the particular case $\sigma_{\mathrm{m}} = 1$) that the steady-state solutions (4.6) and (4.7) are very good approximations.

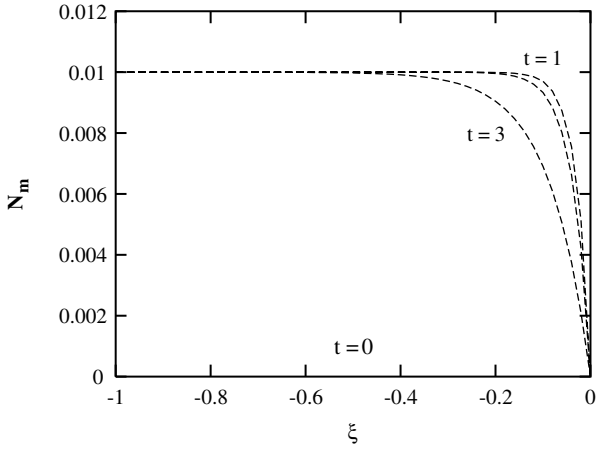

Fig. 7. Transformed concentration on the mask ($\sigma_{\mathrm{m}} = 0.01$).

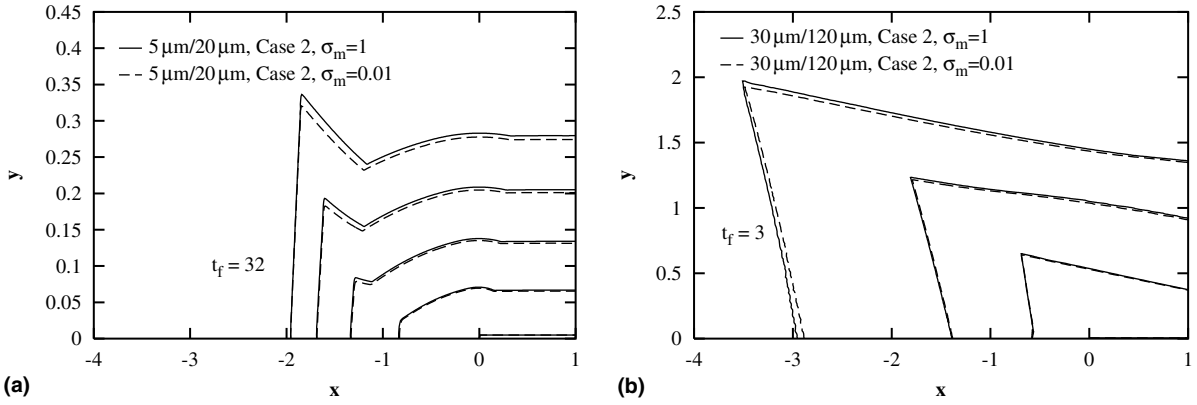

Fig. 8. Comparison of crystal shapes for growth with $\sigma_m = 1.0$,0.01. (a) Narrow geometries. (b) Wide geometries.

Fig. 8 compares the crystal shapes for the Case 2 growth with $\sigma_m = 1.0$ and $\sigma_m = 0.01$. Fig. 8(a) and (b) shows cases of narrow and wide geometries, respectively. The overgrowth rate is insignificantly affected by decrease of the flux from mask through the decrease of sticking coefficient (especially in narrow geometries). It is therefore apparent that surface diffusion channel on the mask provides minor contribution to the total lateral overgrowth rate. Nevertheless, larger values of sticking coefficient result in an increase of both growth rates (same conclusion is drawn in [15]).

5. Conclusions

In this paper, the model for ELO by the combined action of the diffusion in vapor and surface processes (diffusion and evaporation–recondensation) is developed. It is demonstrated computationally, for two distinct and very different modes of anisotropic ELO (and by direct comparisons to the results of the previous model without vapor-phase diffusion, but with the constant precursor flux from vapor and surface processes [18]) that vapor-phase diffusion enhances the lateral overgrowth on the mask and vertical growth. The extent of such enhancement depends strongly on widths of the open stripes and masked portions of the substrate, the enhancement being more pronounced for wide geometries. The influence of the diffusion in vapor on the crystal shapes is small.

A number of recent experimental works on SAG concluded that vapor-phase transport from the regions above the dielectric mask to the exposed regions provides the largest contribution to the *vertical* growth enhancement rate at the boundaries of the exposed regions (Ref. [3] for excellent review and GaN SAG experiment). To the knowledge of the author, for ELO the relative contributions of vapor and surface diffusion were not directly tested experimentally. This work therefore provides a model which allows (under relatively few simplifications) for direct computation of semiconductor ELO and for identification and evaluation of some of the most important physical mechanisms involved in this crystal growth process.

Acknowledgements

Author thanks Professors Richard Braun and Brian Spencer for useful discussions of this work, and the reviewer for a careful review and suggestions.

References

[1] E.J. Thrush, J.P. Stagg, M.A. Gibbon, R.E. Mallard, B. Hamilton, J.M. Jowett, E.M. Allen, Mater. Sci. Eng. B 21 (1993) 130.
[2] New Concepts and Development of Liquid-Phase Electro-Epitaxy for Silicon and III–V Compound Semiconductors, Contract DASG60-92-C-0004, AstroPower, Inc., 24 June 1995, M.G. Mauk, PI.
[3] C.C. Mitchell, M.E. Coltrin, J. Han, J. Cryst. Growth 222 (2001) 144.
[4] M.G. Mauk, J.P. Curran, J. Cryst. Growth 225 (2001) 348.
[5] T. Sasaki, M. Kitamura, I. Mito, J. Cryst. Growth 132 (1993) 435.
[6] J.E. Greenspan, X. Zhang, N. Puetz, B. Emmerstorfer, J. Vac. Sci. Technol. A 18 (2) (2000) 648.
[7] Z.R. Zytkiewicz, J. Domagala, D. Dobosz, J. Appl. Phys 90 (12) (2001) 6140.
[8] O.-K. Nam, T.S. Zheleva, M.D. Bremser, R.F. Davis, J. Electron. Mater. 27 (4) (1998) 233.
[9] Y. Sakata, Y. Inomoto, K. Komatsu, J. Cryst. Growth 208 (2000) 130.
[10] S.C. Lee, L.R. Dowson, S.R.J. Brueck, J. Cryst. Growth 240 (2002) 333–339.
[11] Y. Yamazaki, J.H. Chang, M.W. Cho, T. Sekiguchi, T. Yao, J. Cryst. Growth 214/215 (2000) 202.
[12] X. Mei, M. Blumin, D. Kim, Z. Wu, H.E. Ruda, J. Cryst. Growth 251 (2003) 253–257.
[13] L.J.M. Bollen, C.H.J. Van den Brekel, H.K. Kuiken, J. Cryst. Growth 51 (1981) 581.
[14] M.F. Zybura, S.H. Jones, J.M. Duva, J. Durgavich, J. Electron. Mater. 23 (10) (1994) 1055.
[15] D.J. Coronell, K.F. Jensen, J. Cryst. Growth 114 (1991) 581.
[16] T. Fujii, M. Ekawa, S. Yamazaki, J. Cryst. Growth 146 (1995) 475.
[17] M. Khenner, R.J. Braun, M.G. Mauk, J. Cryst. Growth 235 (2002) 425.
[18] M. Khenner, R.J. Braun, M.G. Mauk, J. Cryst. Growth 241 (2002) 330.
[19] H. Wong, P.W. Voorhees, M.J. Miksis, S.H. Davis, Acta Mater. 48 (2000) 1719.
[20] J.E. Taylor, J.W. Cahn, C.A. Handwerker, Acta. Metall. Mater. 40 (7) (1992) 1443.
[21] T. Nishinaga, in: D.T.J. Hurle (Ed.), Handbook of Crystal Growth, vol. 3, Elsevier Science, 1994, p. 666.
[22] A.A. Chernov, in: D.T.J. Hurle (Ed.), Handbook of Crystal Growth, vol. 3, Elsevier Science, 1994, p. 458.
[23] W.W. Mullins, J. Appl. Phys. 28 (3) (1957) 333.
[24] D.A. Kessler, J. Koplik, H. Levine, Adv. Phys. 37 (1988) 255.
[25] G.B. McFadden, A.A. Wheeler, R.J. Braun, S.R. Coriell, R.F. Sekerka, Phys. Rev. E 48 (3) (1993) 2016.
[26] D. Juric, G. Tryggvason, J. Comput. Phys. 123 (1996) 127.
[27] S. Chen, B. Merriman, S. Osher, P. Smereka, J. Comput. Phys. 135 (1997) 8.
[28] Z. Li, B. Soni, Numer. Ht. Trans. Part B. Fundamentals 35 (1999) 461.
[29] A.A. Golovin, S.H. Davis, A.A. Nepomnyashchy, Physica D 122 (1998) 202.
[30] A. Karma, W.-J. Rappel, Phys. Rev. Lett. 77 (19) (1996) 4050.
[31] R.H. Nochetto, M. Paolini, C. Verdi, SIAM J. Sci. Stat. Comput. 12 (1991) 1207.
[32] V.G. Levich, Physicochemical Hydrodynamics, Prentice-Hall, 1962.
[33] C. Herring, in: R. Gomer, C.S. Smith (Eds.), Structure and Properties of Solid Surfaces, vol. 5, The University of Chicago Press, 1952.
[34] C.A. Brebbia, The Boundary Element Method for engineers, Pentech Press, London, 1984.
[35] E. Hairer, G. Wanner, J. Comput. Appl. Math. 111 (1999) 93.